

Research Paper

Modeling and optimization of gaseous helium (GHe) cooled high temperature superconducting (HTS) DC cables for high power density transmission



N.G. Suttell^a, J.V.C. Vargas^{a,b,*}, J.C. Ordóñez^a, S.V. Pamidi^a, C.H. Kim^a

^a Department of Mechanical Engineering, Energy and Sustainability Center and Center for Advanced Power Systems, Florida State University, Tallahassee, FL 32310–6046, USA

^b Department of Mechanical Engineering, Graduate Program in Materials Science Engineering (PIPE), and Sustainable Energy Research & Development Center (NPDEAS), UFPR – Federal University of Paraná, CP 19011, 81531–980 Curitiba, PR, Brazil

HIGHLIGHTS

- We introduce an HTS DC cable and cryostat transient mathematical model.
- HTS DC cable and cryostat transient temperature distribution is assessed.
- Model adjustment and experimental validation are conducted.
- Total power consumption is estimated based on thermodynamic losses.
- The model allows for system design, control and optimization.

ARTICLE INFO

Keywords:

Energy efficiency improvement
Electricity transmission and distribution
superconducting DC cable internal geometry
Gaseous helium
Experimental validation

ABSTRACT

Superconducting cables are considered a viable technology to meet the increasing global demand of electricity transmission and distribution. This paper presents a transient mathematical model to predict the thermal response of a superconducting cable contained in a flexible cryostat. The model was conceived to be computationally fast so that system response according to variations of physical properties of the materials, and operating and design parameters could be assessed for optimization purposes. A volume element method (VEM) was utilized, which resulted in a system of ordinary differential equations with time as the independent variable. The model is also space dependent, through the establishment of a mesh with a known three-dimensional distribution of the volume elements in the computational domain. Pressure drop in the gas channels and the temperature gradient with respect to space in the flow direction were taken into account. The numerically calculated DC cable heat leak rate under different environmental conditions was initially adjusted and then experimentally validated by direct comparison to actual experimental data. The final part of the study consisted of using the experimentally validated model to perform the DC cable design and operating parameters optimization in order to obtain minimum heat leak rate and pumping power (or total consumed power). By adopting a fixed cable cross sectional area constraint (or total volume for a given length), an optimized helium channels geometry is also found that shows significant improvement in system performance in comparison to an existing system geometry. For example, for a GHe mass flow rate of 3.8 g s^{-1} , the cryostat with the original geometry is shown to consume 20.5% more power than with the optimized geometry. As a result, it is reasonable to state that the combination of accuracy and low computational time allow for the future utilization of the model as a reliable tool for HTS DC cable & cryostat simulation, control, design and optimization purposes.

* Corresponding author at: Department of Mechanical Engineering, Graduate Program in Materials Science Engineering (PIPE), and Sustainable Energy Research & Development Center (NPDEAS), UFPR – Federal University of Paraná, CP 19011, 81531–980 Curitiba, PR, Brazil.

E-mail address: jvargas@demec.ufpr.br (J.V.C. Vargas).

Nomenclature	
A	area, m^2
B	radiosity, W m^{-2}
B_a	bias limit of quantity a
c	specific heat, $\text{J kg}^{-1} \text{K}^{-1}$
c_i	adjustment constants, Eqs. (38) and (39)
d	envelope diameter, m
f	Fanning friction factor
F	view factor, Eq. (21)
h	convection heat transfer coefficient, $\text{W m}^{-2} \text{K}^{-1}$
i	current, A
k	thermal conductivity, $\text{W m}^{-1} \text{K}^{-1}$
L	cable length, m
m	mass flow rate, kg s^{-1}
M	mass, kg
n	exponent, Eq. (4)
n_{VE}	total number of volume elements
Nu	Nusselt number
n_c	number of parallel ducts in gas channel
p	helical pitch, m
P	pressure, N m^{-2}
P_a	precision limit of quantity a
Pr	Prandtl number, ν/α
\dot{Q}	heat transfer rate, W
R	radius, m
Re_{D_h}	Reynolds number based on D_h , uD_h/ν
$S1, \dots, S9$	HTS DC cable and cryostat layers (systems), Fig. 1
t	time, s
T	temperature, K
u	average cross sectional velocity, m s^{-1}
U	global wall heat transfer coefficient, $\text{W m}^{-2} \text{K}^{-1}$
U_a	uncertainty of quantity a
∇	volume, m^3
VE	volume element
W	power, W
x	axial direction, m
$\ \cdot\ $	Euclidean norm of a vector
<i>Greek symbols</i>	
γ	electrical conductivity, $\Omega^{-1} \text{m}^{-1}$
Δp	pressure drop, N m^{-2}
ΔT	temperature difference, K
$\Delta \tau$	dimensionless temperature difference
ΔS	molar entropy change, kJ kmol^{-1}
<i>Subscripts</i>	
0	ambient; initial condition
$1, \dots, 9$	S1 to S9 layers, Fig. 1
b	backward
c	critical
cd	conduction heat transfer
$cons$	consumed
$cryo$	cryostat
cv	convection heat transfer
f	forward
$fluid$	fluid
fr	friction
gen	generation
h	hydraulic
$inlet$	cryostat inlet
$mesh$	mesh
min	minimum
$mylar$	mylar
opt	optimal
$outlet$	cryostat outlet
p	constant pressure
pd	pull-down
rad	radiation heat transfer
ref	reference value
s	cross section
st	stainless steel
tot	total
v	constant volume
$wall$	wall
<i>Superscripts</i>	
(i)	volume element i, $i = 1, \dots, n_{VE}$
\sim	dimensionless variable

1. Introduction

Global energy demands are on the rise, and the current technology used to generate, transmit, and distribute electricity will not be able to meet the growth due to the bottlenecks in densely populated areas and the inefficiencies throughout the electrical grid. Soon, new technologies will be required to relieve the constraints on the grid while being cost effective, reliable, and environmentally acceptable. High temperature superconducting (HTS) technology being developed has the means to provide ways to overcome the challenges faced by electric utility companies [1–3]. Superconducting cables are one of the important power applications of the superconducting technology which is suited for densely populated regions. The main advantage of the High-Temperature Superconducting (HTS) cable is the high current carrying capacity compared to the conventional cable with the same diameter. Therefore, HTS cables could replace the existing Right-of-Way (ROW) aiming at the reduction of cost and environmental impacts of the

network upgrades [2]. Other applications including all-electric ships and aircrafts would also benefit greatly from the use of HTS power devices in meeting the increasing electrical power requirements at high power densities [4–6].

A discussion on applied superconductivity fundamentals is necessary in order to understand the need for appropriate mathematical modeling aiming at energetically efficient and affordable superconducting cables. Several years after the discovery that mercury's electrical resistance dropped to zero at temperatures below 4 K [7], i.e., the so called critical temperature, T_c , two types of superconductors were identified, i.e., I and II, to account for their behavior in applied magnetic fields. The former are mostly elements, and lose superconductivity properties in relatively weak magnetic fields, H_c , to which corresponds a critical current density, J_c [8]. The latter are mostly alloys and compounds, and are capable of displaying the Meissner effect (perfect diamagnetism) under strong magnetic fields. Therefore, in order to exhibit superconductivity the material has to operate below H_c ,

J_c , and T_c , i.e., the so called material superconducting state [8]. Of major importance to the designer of superconducting devices is to ensure that the operating levels are well below their respective critical values to avoid a quench, i.e., a sudden transition from the superconducting state to the normal state that results in rapid Joule heating from the high current, and can potentially damage the device.

Superconducting materials are also categorized as low temperature superconductors (LTS – T_c below 30 K) or high temperature superconductors (HTS – T_c above 30 K) that were discovered in 1986 [9]. All LTS materials obey the Bardeen-Cooper-Schrieffer (BCS) theory of superconductivity [8], which explains superconductivity based on quantum mechanics and on the attraction of electrons into pairs called Cooper pairs that remain paired at low temperatures. However, HTS materials have yet no microscopic explanation as to how they work and their superconducting properties are highly anisotropic making it more difficult to design HTS devices [8]. The primary advantage of using HTS over LTS devices for electric power applications is the improved refrigeration efficiency since as temperature approaches the absolute

zero, refrigeration efficiency drops rapidly, approaching zero as well. The Carnot coefficient of performance defines the theoretical maximum efficiency of a cryocooler, and is directly proportional to cooling temperature. For example, The Carnot COP of a cryocooler is 1.4% operating at the liquid helium (LHe) temperature of 4.2 K and dumping heat at 300 K (room temperature). That COP value rises to 34% if the cryocooler is operating at the liquid nitrogen (LN₂) boiling point of 77 K [10]. Additionally, the specific heat of solid materials at cryogenic temperatures varies as T^3 [8]. In other words, HTS devices have a much better thermal stability than LTS systems because a significantly larger heat disturbance is required to quench an HTS system.

HTS materials are additionally classified as first and second generation. The Bi₂Sr₂Ca₂Cu₃O₁₀ (BSCCO 2223) superconductor is considered a first generation (1G) HTS because it was the first commercially available HTS material in long lengths [9]. The fabrication of 1G HTS tapes is based on the “powder-in-tube” process [11]. The YBa₂Cu₃O₇ (YBCO-123), generally known as REBCO, is considered the second generation (2G) HTS because it became available later, and the

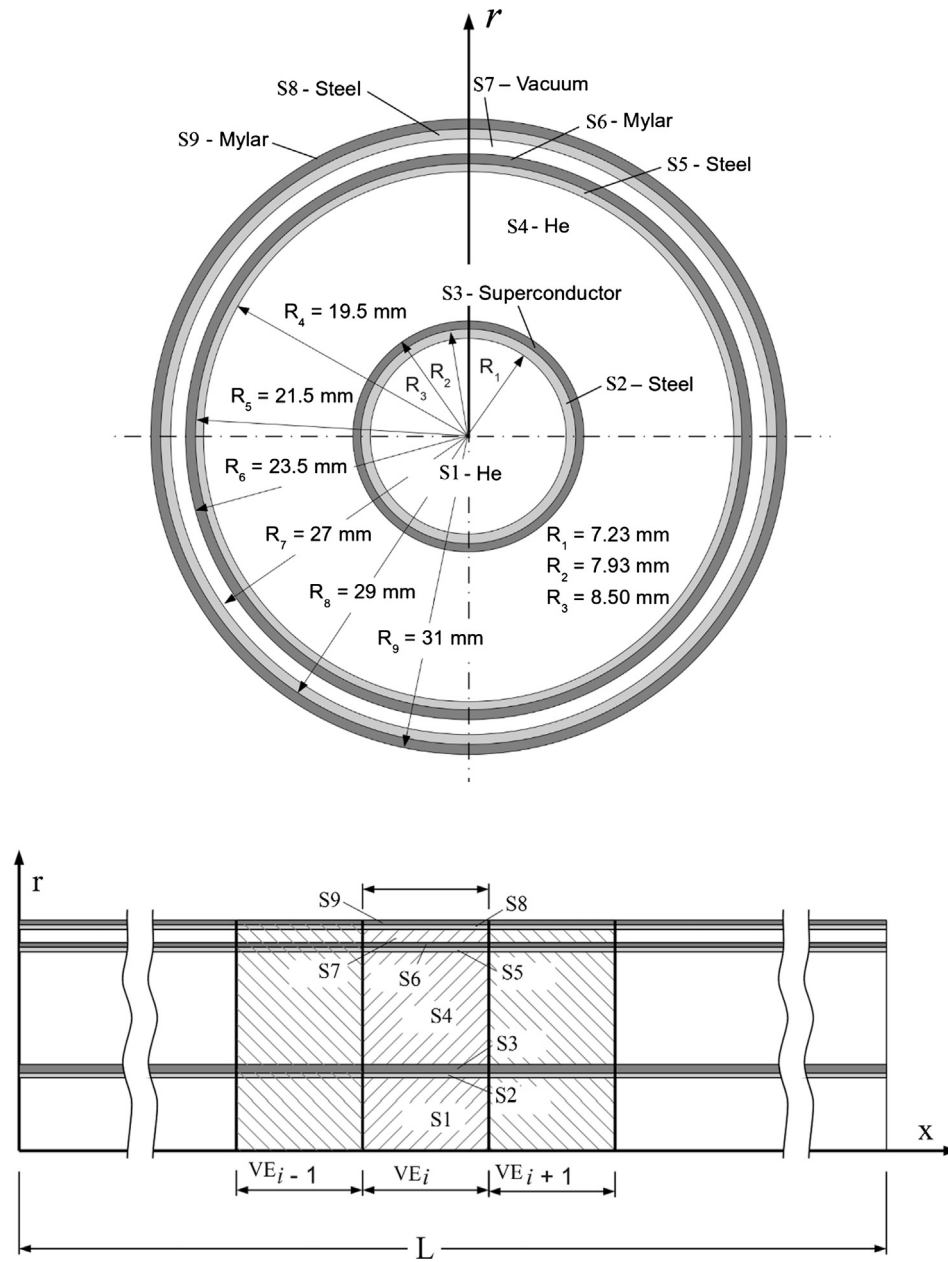


Fig. 1. The superconducting cable cross sectional area layers distribution (top) in the radial direction and the volume elements in the longitudinal direction (bottom).

long length is fabricated commercially using a few different thin film deposition techniques. The REBCO family of HTS have a T_c onset of 93 K making it the first HTS discovered with T_c values above the liquid nitrogen boiling temperature [9]. The current record holder for the highest T_c is the Hg-Ba-Ca-Cu-O system reaching 135 K at ambient pressure and 160 K under high pressure [12]. Such materials can carry up to 150 times the electrical current of equivalently-sized copper wire [13]. There are a few recent HTS AC cable projects that have been successfully tested [14–20]. All HTS cable projects until now have been partly supported by government funding. For a truly commercial HTS AC cable to happen, cost needs to be reduced. There is steady progress in materials science and manufacturing processes to bring down the price of 2G HTS tapes [21–25]. Additionally, HTS devices' cost could be reduced by increasing the cryogenic thermal efficiencies thereby minimizing the required quantity of HTS material used in each application by operating at lower temperatures.

So far in this discussion of applied superconductivity fundamentals, it is reasonable to state that the success of the technology will rely upon HTS cables. In such scenario the natural question is what sort of HTS cable would be more recommendable among the currently known technologies. Gaseous helium (GHe) could prove more beneficial over LN₂, since it could reach lower temperatures than LN₂ allowing a higher J_c in the HTS wire, hence requiring less material for the same application. According to Eckroad [26], a 3 K temperature reduction can result in a 20% decrease in the required amount of superconducting material. However, intensive modeling and experimentation must be performed to understand the implications of using gaseous helium for large HTS devices [27–29]. A 2G HTS tape at 20 K can carry six to eight times the current it can carry at 77 K [30]. It is also possible to modify the power capacity rating of a GHe-cooled cable through a wide range as needed simply by changing its operating temperature. This way, it would only be necessary to operate the cable at relatively lower temperatures during peak power demands.

The US Navy has been interested in cryogenic GHe research for applications including HTS degaussing systems, propulsion motors and generators, and power cables for future all-electric naval ships [31,32]. A superconducting integrated power system (SIPS) based on HTS technology is desired to reap the benefits of HTS technology [33]. A SIPS on a naval ship would allow powering HTS degaussing systems, generators, and propulsion motors all on the same superconducting power distribution network while simultaneously powering other ship services, radar, and directed energy weapons. Therefore, much research has been conducted with the goal of improving GHe HTS cryogenic systems [34–39], and thermal mapping of the entire HTS cable system including the terminations [40,41]. An HTS cable mathematical model that allow for the computational simulation of temperature rise and pressure drop of the cryogenic GHe through the cable has been developed [42]. The combined thermal and electrical analysis has also been performed on similar systems [43].

The next question to address is whether to adopt HTS AC or DC transmission and distribution cables to full commercial initiation among all HTS power applications. HTS AC cables experience losses due to AC losses that include flux-transfer loss, hysteretic loss, and eddy current loss. Currently, however, HTS AC cables are more commercially viable than DC because most of the existing power grid today is AC, and because the high energy and monetary costs of AC-DC conversion would be considerably higher than the cost of just AC losses [44]. HTS DC cables are similar to AC cables. The biggest difference is that DC cables have two poles: a positive and a negative pole, while AC cables have three phases and a shield or return phase. Additionally, HTS DC cables have lower electrical loss than AC cables, and because of this they have the opportunity of replacing transmission cables hundreds of kilometers long to connect renewable energy sources. In the case of a DC grid, there would not have to be any AC-DC conversion between the power generation source and homes and devices. Because DC cables can transport large amounts of current with limited power dissipation, they

are strong candidates for applications such as electrical ships and aircrafts, railway grids, and renewable energy facilities [8].

Based on the applied superconductivity challenges discussed so far in the bibliographic review, it is reasonable to state that much research on superconducting cables optimal thermal design is still needed, whose results would greatly contribute to the system future technical and economic viability. Therefore, in this paper, a study on mathematical modeling, experimental validation and optimization of GHe cooled superconducting DC cables is conducted.

2. Mathematical model

For the sake of generality, the DC cable and cable cryostat are modeled nondimensionally. The DC and cable cryostat are divided into Volume Elements (VE) in the x (axial) direction, and the cross section in systems in the r (radial) direction, as shown in Fig. 1 (top). Each volume element is composed by nine layers (systems), corresponding to the structure of an experimental superconducting DC cable under study at the Center for Advanced Power Systems (CAPS), FSU: internal helium channel (S1), stainless steel structural pipe (S2), superconducting cable (S3), external annular helium channel (S4), stainless steel (S5), Mylar insulation (S6), vacuum (S7), stainless steel (S8) and Mylar (S9). The bottom part of Fig. 1 illustrates the discretization in the x (axial) direction.

The model neglects channels spacers that also act as supporting structure assuming they are small enough not to affect the cable thermal response. Parallel flow is assumed for helium in S1 and S4. However, if counterflow is adopted, one of the channels could be used for recirculation. The dielectric material that actually exists in the system (thin layers between S2, S3 and S4) is also neglected.

The mathematical model is constructed based on the application of the first law of thermodynamics to all systems (S1 to S9) in each VE. Constitutive equations are used to evaluate the physical properties, and theoretical and empirical correlations used to calculate heat transfer rates between the VE. Accordingly, the model previously presented by the same authors of this study [42,45] is amended and herein non-dimensionalized.

S1 – Internal helium channel

The First Law of Thermodynamics applied to S1 states that

$$\frac{\partial \tau_1^{(i)}}{\partial \tilde{t}} = \{-\tilde{Q}_{cv,1,2}^{(i)} + \psi_1(\tau_1^{(i-1)} - \tau_1^{(i)}) - \tilde{W}_{fr,1}^{(i)}\} \frac{1}{\tilde{M}_1^{(i)} \tilde{c}_{v,1}} \quad (1)$$

where $i = 1, \dots, n_{VE}$, n_{VE} is the total number of volume elements, and dimensionless groups are defined as follows:

$$\begin{aligned} (\tilde{Q}, \tilde{W}) &= \left(\frac{\dot{Q}, \dot{W}}{h_{ref} AT_0} \right); \quad \tau_j = \frac{T_j}{T_0}; \quad \tilde{t} = \frac{t}{(M_{ref} c_{st,0})/(h_{ref} A)}; \quad \tilde{M}_j \\ &= \frac{M_j}{M_{ref}}; \quad \psi_j = \frac{(mc_p)_j}{h_{ref} A}; \quad (\tilde{x}, \tilde{R}) = \frac{(x, R)}{L}; \quad \tilde{c}_{a,j} = \frac{c_{a,j}}{c_{st,0}} \quad \text{for } j \\ &= 1, \dots, 9 \end{aligned} \quad (2)$$

where h_{ref} , and M_{ref} are appropriate scales for the convection heat transfer coefficient and mass; $A = \pi R_s^2$ the total cable section area; T_0 the surrounding environment temperature; $c_{st,0}$ the stainless steel specific heat at T_0 ; subscript a refers to constant volume or pressure (a) for the fluid ($j = 1$ and 4), and is not used for the solid layers, and subscript j refers to the substance in a particular system (j).

Additionally, the convective heat transfer rate between systems j and $j + 1$ is calculated as follows:

$$\dot{Q}_{cv,j,j+1}^{(i)} = h_j A_{j,j+1}^{(i)} (T_j^{(i)} - T_{j+1}^{(i)}) \quad (3)$$

$$\text{where } A_{j,j+1}^{(i)} = 2\pi R_j \Delta x^{(i)}.$$

The convective heat transfer coefficient, h , was evaluated for both

laminar and turbulent regimes. For the latter, the Dittus-Boelter correlation was used [46,47], which has been applied before for cryogenic conditions [48]:

$$\begin{cases} Nu_{D_h} = 4.36 \text{ (Laminar - constant heat flux)} \\ Nu_{D_h} = 0.023 Re_{D_h}^{0.8} Pr^n \text{ (Turbulent)} \end{cases} \quad (4)$$

where Nu_{D_h} is the Nusselt number, and Re_{D_h} the Reynolds number, both based on D_h the hydraulic diameter ($2500 \leq Re_{D_h} \leq 1.24 \times 10^5$); Pr the fluid Prandtl number ($0.7 \leq Pr \leq 120$), and $n = 0.4$ when $T_{\text{wall}} > T_{\text{fluid}}$ and $n = 0.3$ when $T_{\text{wall}} < T_{\text{fluid}}$, and $L/D_h > 60$ [47].

As a result, the convective heat transfer coefficient in system j, h_j , is then calculated by

$$h_j = \frac{k_j Nu_{D_h,j}}{D_{h,j}} \quad \text{and } j = 1 \text{ or } 4 \quad (5)$$

The power to overcome friction in system (channel) j for VE i is calculated as follows:

$$\dot{W}_{fr,j}^{(i)} = \frac{\dot{m}_j \Delta p_j^{(i)}}{\rho_j} \quad (6)$$

in which the pressure drop is calculated for $j = 1$ and 4 with

$$\Delta p_j^{(i)} = f_j \frac{4 \Delta x^{(i)}}{D_{h,j}} \frac{1}{2} \rho_j u_j^2 \quad (7)$$

where for the laminar regime, $Re \leq 2300$, the Fanning friction factor is calculated as follows [46]:

$$f_j = 16 Re_{D_h,j} \quad (8)$$

and for the turbulent regime, $Re > 2300$, for system 1 ($j = 1$) the Fanning friction factor for a smooth pipe is calculated using the Petukhov correlation [46] as follows:

$$f_1 = \frac{1}{4} (0.790 \ln Re_{D_h,1} - 1.64)^{-2} \quad (9)$$

with

$$Re_{D_h,j} = \frac{u_j D_{h,j}}{\nu_j}; \quad u_j = \frac{\dot{m}_j}{\rho_j A_{s,j}} \quad \text{and } j = 1 \text{ or } 4 \quad (10a)$$

and noting that pressure and temperature are assumed uniform in the horizontal chamber of termination 1 of the GHe HTS DC cable and cryostat system shown in Fig. 2, helium density and velocity are the

same at S1 and S4 inlets. Therefore, taking into account mass conservation, the total helium mass flow rate that enters the cryostat is distributed to S1 and S4 as follows:

$$\dot{m} = \dot{m}_1 + \dot{m}_4; \quad \frac{\dot{m}_1}{\dot{m}_4} = \frac{A_1}{A_4} \quad \text{so that} \quad \begin{cases} \dot{m}_1 = \dot{m}/[1 + 1/(A_1/A_4)] \\ \dot{m}_4 = \dot{m} - \dot{m}_1 \end{cases} \quad (10b)$$

S2 – Structural stainless steel

The First Law of Thermodynamics applied to S2 states that

$$\frac{\partial \tau_2^{(i)}}{\partial t} = \{\tilde{Q}_{cv,1,2}^{(i)} + \tilde{Q}_{cd,2,3}^{(i)} + \tilde{Q}_{cd,b,2}^{(i)} + \tilde{Q}_{cd,f,2}^{(i)}\} \frac{1}{\tilde{M}_2^{(i)} \tilde{c}_2^{(i)}} \quad (11)$$

where

$$M_2^{(i)} = \rho_{st} \nabla_2^{(i)}; \quad \forall_j^{(i)} = A_{s,j} \Delta x^{(i)}; \quad A_{s,j} = \pi (R_j^2 - R_{j-1}^2) \quad \text{for } j \geq 2 \quad (12)$$

The radial conduction heat transfer rate between systems j and $j + 1$ is calculated as follows:

$$\begin{aligned} \dot{Q}_{cd,j,j+1}^{(i)} &= (UA)_{j,j+1}^{(i)} (T_{j+1}^{(i)} - T_j^{(i)}); \quad (UA)_{j,j+1}^{(i)} \\ &= \left\{ \frac{\ln \left(\frac{2R_j}{R_{j-1} + R_j} \right)}{2\pi k_j \Delta x^{(i)}} + \frac{\ln \left(\frac{R_j + R_{j+1}}{2R_j} \right)}{2\pi k_{j+1} \Delta x^{(i)}} \right\}^{-1} \end{aligned} \quad (13)$$

The longitudinal conduction heat transfer rates between systems j, VE i, and the backward (b), VE $i - 1$, and forward (f), VE $i + 1$, are calculated as follows:

$$\dot{Q}_{cd,b,j}^{(i)} = -\frac{k_j A_{s,j} (T_j^{(i)} - T_{j-1}^{(i)})}{\Delta x^{(i)}/2 + \Delta x^{(i-1)}/2}; \quad \dot{Q}_{cd,f,j}^{(i)} = -\frac{k_j A_{s,j} (T_j^{(i)} - T_{j+1}^{(i)})}{\Delta x^{(i)}/2 + \Delta x^{(i+1)}/2} \quad (14)$$

S3 – Superconductor

The First Law of Thermodynamics applied to S3 states that

$$\frac{\partial \tau_3^{(i)}}{\partial t} = \{-\tilde{Q}_{cv,3,4}^{(i)} - \tilde{Q}_{cd,2,3}^{(i)} + \tilde{Q}_{cd,b,3}^{(i)} + \tilde{Q}_{cd,f,3}^{(i)} + \tilde{Q}_{gen}^{(i)}\} \frac{1}{\tilde{M}_3^{(i)} \tilde{c}_3^{(i)}} \quad (15)$$

where

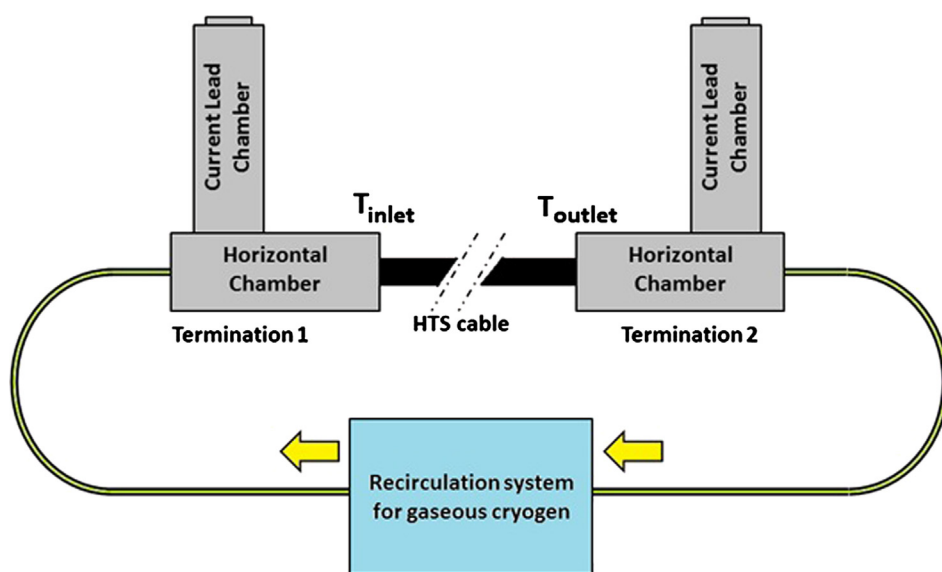


Fig. 2. Schematic diagram of HTS cable and cryogenic helium gas circulation system.

$$\dot{Q}_{gen}^{(i)} = \frac{1}{\gamma_3} \frac{\Delta x^{(i)}}{A_{s,2}} i^2 \quad (16)$$

S4 – Annular helium channel

The First Law of Thermodynamics applied to S4 states that

$$\frac{\partial \tau_4^{(i)}}{\partial t} = \{\tilde{Q}_{cv,3,4}^{(i)} - \tilde{Q}_{cv,4,5}^{(i)} + \psi_4 (\tau_4^{(i-1)} - \tau_4^{(i)}) - \tilde{W}_{fr,4}^{(i)}\} \frac{1}{\tilde{M}_4^{(i)} \tilde{c}_{v,4}^{(i)}} \quad (17)$$

where $\tilde{W}_{fr,4}^{(i)}$ is calculated with Eqs. (6)–(10), in which for system 4 ($j = 4$) the Fanning friction factor for the turbulent regime, $Re_{D_h} > 2300$, for spirally corrugated channels is calculated using the following experimental correlation [49]:

$$f_4 = \frac{1}{4} (1.53 \phi^{0.46} Re_{D_h,4}^{-0.16}) \quad (18)$$

in which $\phi = \frac{h^2}{pd}$ is the severity factor for corrugated tubes, being the ratio of the square of the roughness height, h , to the product of the helical pitch, p , and the envelope diameter [49]. There is a reported 7% error for 95% of the experimental data for $8000 \leq Re_{D_h} \leq 60,000$, and for $2000 \leq Re_{D_h} < 8000$, it is recommended the use of a constant friction factor evaluated with Eq. (8) with $Re_{D_h} = 8000$ [49].

S5 – Structural stainless steel

The First Law of Thermodynamics applied to S5 states that

$$\frac{\partial \tau_5^{(i)}}{\partial t} = \{\tilde{Q}_{cv,4,5}^{(i)} + \tilde{Q}_{cd,5,6}^{(i)} + \tilde{Q}_{cd,b,5}^{(i)} + \tilde{Q}_{cd,f,5}^{(i)}\} \frac{1}{\tilde{M}_5^{(i)} \tilde{c}_5^{(i)}} \quad (19)$$

S6 – Mylar

The First Law of Thermodynamics applied to S5 (Mylar insulation layer) states that

$$\frac{\partial \tau_6^{(i)}}{\partial t} = \{-\tilde{Q}_{cd,5,6}^{(i)} + \tilde{Q}_{cd,b,6}^{(i)} + \tilde{Q}_{cd,f,6}^{(i)} + \tilde{Q}_{rad,6}^{(i)}\} \frac{1}{\tilde{M}_6^{(i)} \tilde{c}_6^{(i)}} \quad (20)$$

in which, the last term between the curly brackets that accounts for the radiation heat transfer rate experienced by S6 is calculated for the interaction between two concentric circular surfaces, $A_{6,7}^{(i)}$ and $A_{7,8}^{(i)}$, so that the angle (or view) factors are given by [50]

$$F_{6,8} = 1; \quad F_{8,6} = \frac{A_{6,7}^{(i)}}{A_{7,8}^{(i)}}; \quad F_{6,6} = 0; \quad \text{and} \quad F_{8,8} = 1 - \frac{A_{6,7}^{(i)}}{A_{7,8}^{(i)}} \quad (21)$$

An enclosure is defined by system 7 which is bounded by two grey surfaces, $A_{6,7}^{(i)}$ and $A_{7,8}^{(i)}$. In order to calculate the radiant interchange at the surfaces, the enclosure concept is utilized [50]. Based on that, the two surfaces radiosities (total radiation heat flux that leaves each surface) are calculated by solving the following system of equations:

$$\begin{cases} B_6 = \varepsilon_6 \sigma (T_6^{(i)})^4 + (1-\varepsilon_6) (B_6 F_{6,6} + B_8 F_{6,8}) \\ B_8 = \varepsilon_8 \sigma (T_8^{(i)})^4 + (1-\varepsilon_8) (B_6 F_{8,6} + B_8 F_{8,8}) \end{cases} \quad (22)$$

whose solution is obtained analytically, and given by

$$B_6 = \varepsilon_6 \sigma (T_6^{(i)})^4 + (1-\varepsilon_6) B_8 \quad (23)$$

where

$$B_8 = \frac{\varepsilon_8 \sigma (T_8^{(i)})^4 + (1-\varepsilon_8) \varepsilon_6 \sigma (T_6^{(i)})^4}{1 - F_{8,8} (1-\varepsilon_8) (1-\varepsilon_6) F_{8,6}} \quad (24)$$

Finally, a balance of energy in each surface states that:

$$\dot{Q}_{rad,6}^{(i)} = -\frac{\varepsilon_6}{1-\varepsilon_6} A_{6,7} \{ \sigma (T_6^{(i)})^4 - B_6 \} \quad (25)$$

$$\dot{Q}_{rad,8}^{(i)} = -\frac{\varepsilon_8}{1-\varepsilon_8} A_{7,8} \{ \sigma (T_8^{(i)})^4 - B_8 \} \quad (26)$$

S7 – Vacuum

Since the space is evacuated, no energy equation is written for S7. However, the space is crossed by a radiation heat transfer rate between S6 and S9.

S8 – Structural stainless steel

The First Law of Thermodynamics applied to S2 states that

$$\frac{\partial \tau_8^{(i)}}{\partial t} = \{\tilde{Q}_{rad,8}^{(i)} + \tilde{Q}_{cd,8,9}^{(i)} + \tilde{Q}_{cd,b,8}^{(i)} + \tilde{Q}_{cd,f,8}^{(i)}\} \frac{1}{\tilde{M}_8^{(i)} \tilde{c}_8^{(i)}} \quad (27)$$

S9 – Mylar

The First Law of Thermodynamics applied to S9 (Mylar insulation layer) states that

$$\frac{\partial \tau_9^{(i)}}{\partial t} = \{-\tilde{Q}_{cd,8,9}^{(i)} + \tilde{Q}_{cd,b,9}^{(i)} + \tilde{Q}_{cd,f,9}^{(i)} + \tilde{Q}_0^{(i)}\} \frac{1}{\tilde{M}_9^{(i)} \tilde{c}_9^{(i)}} \quad (28)$$

in which, the last term between the curly brackets that accounts for the heat transfer rate with the external environment is calculated by

$$\dot{Q}_0^{(i)} = (UA)_{9,0}^{(i)} (T_0^{(i)} - T_g^{(i)}) \quad (29)$$

where

$$(UA)_{9,0}^{(i)} = \left\{ \frac{\ln \left(\frac{2R_9}{R_8 + R_9} \right)}{2\pi k_9 \Delta x^{(i)}} + \frac{1}{A_{9,0}^{(i)} h_0} \right\} \quad (30)$$

2.1. Thermophysical properties

The mathematical model requires the evaluation of the thermodynamic properties of helium (ρ , c_p and c_v) which were calculated as functions of temperature, T , and pressure, P using appropriate equations of state [51]. The helium viscosity and thermal conductivities were also evaluated based on available documented data [52]. The structural pipes are made with stainless steel S316, so that the specific heat and thermal conductivity at cryogenic conditions were calculated as functions of temperature from empirical correlations [53]. The stainless steel S316 density and emissivity were considered constant and equal to 7970 kg/m^3 [46] and 0.12 [50], respectively. The Mylar thermal conductivity was evaluated as a function of temperature [54], whereas density, specific heat and emissivity were taken as $\rho_{\text{mylar}} = 1390 \text{ kg m}^{-3}$ [55], $c_{\text{mylar}} = 1170 \text{ J kg}^{-1} \text{ K}^{-1}$ [55] and $\varepsilon_{\text{mylar}} = 0.03$ [56], respectively. The experimental system considered in this study uses the compound yttrium barium copper oxide, $\text{YBa}_2\text{Cu}_3\text{O}_7$ (YBCO-123) as the superconducting material whose thermophysical properties were obtained from the technical literature [57].

2.2. Optimization problem formulation

In order to evaluate the superconducting cable performance, two aspects are taken into account: (i) the required cryocooling power, and (ii) the required pumping power to overcome friction at the steady state. Mathematically, such values are assessed with the model as follows:

$$\tilde{Q}_{\text{ryo}} = \psi_1 (\tau_1^{(\text{nVE})} - \tau_1^{(1)}) + \psi_4 (\tau_4^{(\text{nVE})} - \tau_4^{(1)}) \quad (31)$$

$$\tilde{W}_{fr,tot} = \sum_{i=1}^{nVE} (\tilde{W}_{fr,1}^{(i)} + \tilde{W}_{fr,4}^{(i)}) \quad (32)$$

Therefore, the performance objective function to be minimized is the superconducting cable total consumed power, which is given by the sum of the two quantities as follows:

$$\tilde{W}_{\text{cons}} = \tilde{Q}_{\text{cryo}} + \tilde{W}_{\text{fr,tot}} \quad (33)$$

The formulation is completed by recognizing that the superconducting cable section area, A, needs to be constrained due to a limited space availability wherever the cable is to be mounted. In order to enforce the area constraint according to the cryostat geometry presented in Fig. 1, the optimization procedure is conducted for fixed dimensionless cryostat outer radius \tilde{R}_9 .

The solution to the optimization problem formulated by Eq. (33) and the constrained superconducting cable section area consists of finding optimal geometric and operating parameters that minimize \tilde{W}_{cons} .

3. Numerical method

Eqs. (1), (11), (15), (17), (19), (20), (27) and (28) for dimensionless temperatures, auxiliary algebraic equations, and the specified initial conditions form a system of $8 \times n_{VE}$ ordinary differential equations (ODE), which is the initial value problem to be solved. The unknowns are $\tau_j^{(i)}$ ($i = 1, \dots, n_{VE}; j = 1, \dots, 9, j \neq 7$), i.e., the temperatures in the n_{VE} control volumes. Once the temperatures are known, the required cryocooling power, and pumping power to overcome friction are calculated for any system geometric and operating configuration.

Two numerical methods were used. The first method calculates the transient behavior of the system, starting from a set of initial conditions, then the solution is marched in time (and checked for accuracy) until a steady state is achieved. The equations are integrated in time explicitly using an adaptive time step, 4th-5th order Runge-Kutta method [58]. The time step is adjusted automatically according to the local truncation error, which is kept below a specified tolerance of 10^{-6} . The integration time was the time to achieve steady state, i.e., when the norm of the six variables no longer changed in time according to a pre-specified tolerance, i.e., $d \|\vec{\tau}\| / d\tilde{t} \leq 10^{-2}$, $\vec{\tau} = (\tau_j^{(1)}, \dots, \tau_j^{(n_{VE})})^T$ where ($j = 1, \dots, 9, j \neq 7$).

The second method is used to obtain the steady-state solution directly in order to expedite the optimization study. The time derivatives

are dropped from Eqs. (1), (11), (15), (17), (19), (20), (27) and (28). The system reduces to $8 \times n_{VE}$ nonlinear algebraic equations, in which the unknowns are the temperatures of the 8 systems shown in Fig. 1 for the n_{VE} control volumes. This system is solved using a quasi-Newton method [58]. Convergence was achieved when the Euclidean norm of the residual of the system was less than 10^{-6} .

Mesh convergence was assessed according to well established policies for scientific publications as follows [59]:

$$\lambda_{\text{mesh}} = \frac{|\tau_{\text{outlet,mesh},k} - \tau_{\text{outlet,mesh},k+1}|}{\tau_{\text{outlet,mesh},k}} \leq 0.01 \quad (34)$$

in which λ_{mesh} is the relative error of the helium cryostat outlet dimensionless temperature, τ_{outlet} , between a more (mesh $k + 1$) and a less (mesh k) refined mesh, so that mesh k is utilized when the criterion is satisfied.

The cryostat inlet temperature is an input for the mathematical model, and the outlet temperature results from the mixing of the GHe mass flow rates coming out of S1 and S4. Therefore, a balance of energy at the cryostat outlet states that the dimensionless cryostat outlet temperature is given by:

$$\tau_{\text{outlet}} = \frac{\dot{m}_4 \tau_4^{(n_{VE})} + \dot{m}_1 \tau_1^{(n_{VE})}}{\dot{m}} \quad (35)$$

in which $\tau_4^{(n_{VE})}$ and $\tau_1^{(n_{VE})}$ are calculated by the mathematical model presented in Section 2.

4. Experimental GHe-Cooled HTS cable test bed

4.1. Experimental set up

Florida State University Center for Advanced Power Systems (FSU-CAPS) is the home of a versatile test bed and consists of large cryogenic helium circulation systems connected to a 30-m long cable cryostat and the cable terminations that utilizes the superconducting material YBCO. The test bed has been extensively instrumented and has been used for several previous HTS cable studies [30,34–41,43]. Fig. 2 shows a schematic diagram of the 30-m test cable and the closed loop GHe circulation system. The 30-m HTS cable was designed and manufactured in collaboration with Ultera Systems, Inc., and uses the cable

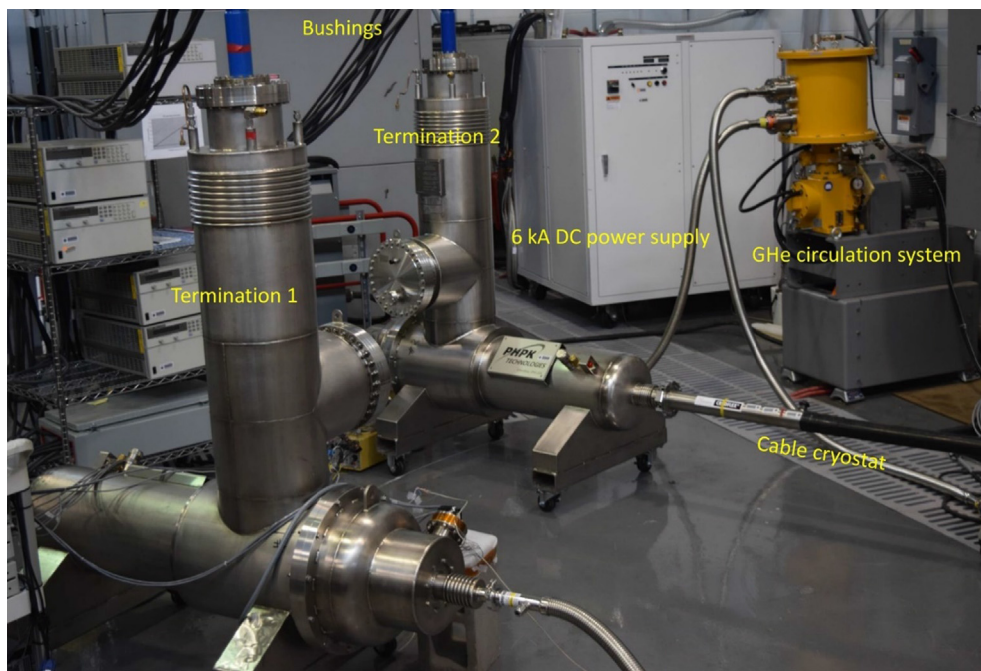


Fig. 3. HTS DC 30 m test cable system located at FSU-CAPS.

cryostat that was procured from Nexans Deutschland GmbH. Each end of the HTS cable is a termination containing the copper current lead/HTS interface as well as GHe inlet and outlet ports within a vacuum jacketed cryogenic environment. Cryogenic GHe enters the termination 1 from the left in Fig. 2 at around 45–50 K at a mass flow rate of 8 g s^{-1} typically, and it cools the copper lead and HTS contacts. The gas traverses the cable system to the right along with the HTS cable and travels through the 30-m cable cryostat extracting heat leaking in through the insulation before entering termination 2. GHe performs the same task in termination 2 as in termination 1. The purpose of the GHe is to absorb the heat that leaks through the thermal insulation and that generates due to Joule heating from the copper leads and electrical contacts. After flowing through the cable system, the warmed up GHe enters the heat exchangers in the cryogenic refrigeration system. The cryogenic helium circulation system is comprised of a cryocooler, a heat exchanger attached to the cold head, and a cryogenic gas impeller. Both a single-stage Stirling cryorefrigerator and a multi-unit Cryomech cryocoolers have been used in the cable system.

CAPS has successfully demonstrated the HTS cable system at an operating current of 3 kA at 77 K and at 6 kA at an operating temperature of 65 K. CAPS has participated in the development of design variations of GHe-cooled HTS DC and AC cables to understand their dielectric and thermal aspects [30]. The dielectric design has been validated by up to 3.5 kV through high-voltage DC soak tests [34].

Fig. 3 shows the layout of the HTS cable and the cryogenic circulation system at CAPS. Cryogenic thermal maps of the system were developed by gathering data recorded by temperature sensors located at several different locations within the terminations. The inlet and outlet temperatures of the cable are also recorded. Combining these data with those of the mass flow rate measurement devices and pressure sensors, an accurate estimation of the heat leak can be calculated. Previous results show a temperature rise across the cable system of 3 K at a GHe mass flow rate of 8.6 g s^{-1} and a load current of 3 kA [40]. The time and cost associated with setting up and completing these experiments can be demanding. This is one of the primary reasons behind the efforts to develop accurate numerical models aiming at the design, control and optimization of such systems. In this study, experimental data collected from the test system were utilized to experimentally adjust and validate the mathematical model developed in Section 2.

There are four ways heat can leak into an HTS cable system: (i) heat generation from non-ideal superconducting material; (ii) heat leak through the cryogenic envelope; (iii) Joule dissipation and thermal conduction through the terminations, cryofans, current leads, and joints, and (iv) AC losses due to ripples and harmonics. The mathematical model proposed in Section 2 accounts for losses of types (i) and (ii) associated with the HTS DC cable and cable cryostat.

4.2. Experimental procedure and uncertainty analysis

The test bed described in the previous section was used to gather the experimental data set required for the experimental validation of the mathematical model introduced in this study. Each test consisted of measuring the values of temperatures, pressures and mass flow rates in order to quantitatively describe the performance of the HTS DC cable based on the objective function definition presented in Eq. (33). This was done by calculating the superconducting cable total consumed power, \tilde{W}_{cons} , using the necessary experimentally measured physical quantities according to Eqs. (31)–(33), for different system helium mass flow rate operating conditions.

The experimental work involved the acquisition of the system physical quantities output data in real time. This task was performed through the utilization of a computational data acquisition system manufactured by National Instruments, USA, which allowed for the sequential data acquisition at interval times of 0.1 s. All the data were processed by a suitable software application to convert the signals into temperatures, pressures and mass flow rates readings.

The calculation of experimental uncertainties is essential for the adequate evaluation of the obtained results. Through the temperatures, pressures and mass flow rates measurements during the transient evolution of the system and at steady state conditions, it is sought to experimentally determine how the system is affected by the variation of helium mass flow rate in terms of power consumption. Such results contain uncertainties due to the measurement process and instrumentation that need to be quantified.

The average of the measurements taken in all runs was utilized to estimate system power consumption. The precision limit of the measurements was calculated as twice the standard deviation of the experimental runs for measuring quantity a , $2\sigma_a$, assuming that the population follows a symmetric unimodal normal distribution, within a 95% confidence interval [60].

In this work, the physical quantities measurements uncertainties were estimated according to standard criteria from the American Society of Mechanical Engineers, ASME [61]. The measurements uncertainties are therefore obtained as follows:

$$U_a = \sqrt{P_a^2 + B_a^2} \quad \text{or} \quad \frac{U_a}{a} = \sqrt{\left(\frac{P_a}{a}\right)^2 + \left(\frac{B_a}{a}\right)^2} \quad (36)$$

where B_a is quantity a 's bias limit, and P_a the precision limit, i.e., $2\sigma_a$. Therefore, U_a is quantity a 's measurements uncertainty.

5. Results and discussion

In this section, the HTS DC cable and cryostat behavior is studied experimentally and numerically, considering the superconductor material YBCO. Test bed measurements are used to experimentally validate the numerical results obtained with the mathematical model introduced in Section 2, using 2 (two) different sets of measured data obtained for the system shown in Fig. 2 for a number of different GHe mass flow rates. The procedure consists of solving the inverse problem of parameters estimation to calculate model adjustment constants using the conditions of the first data set, therefore adjusting the mathematical model. After that, the conditions corresponding to the second data set are computationally simulated with the adjusted model to verify the agreement between numerical and experimental results. Finally, the experimentally validated model is used to investigate the HTS DC cable and cryostat transient temperature distribution and optimize operating and geometric parameters for minimum steady state superconducting cable total consumed power according to Eq. (33).

5.1. Model experimental validation

A computational code was written in Fortran language based on the numerical method described in Section 3 to obtain the solution to the HTS DC cable and cryostat mathematical model, i.e., temperatures and pressure drops, and then computing the superconducting cable total consumed power for the entire GHe mass flow rate operating range. The input parameters are the geometric features, operating parameters and physical properties of the HTS DC cable and cryostat. The geometry was measured directly from the HTS DC cable and cryostat in the laboratory with $L = 30 \text{ m}$, and is shown in Fig. 1. The utilized operating parameters include the ambient temperature, $T_0 = 298.15 \text{ K}$, the inlet temperature, T_{inlet} , and total helium gas mass flow rate, \dot{m} , which were varied in the ranges ($45 \text{ K} \leq T_{\text{inlet}} \leq 52 \text{ K}$) and ($0.5 \text{ g s}^{-1} \leq \dot{m} \leq 10 \text{ g s}^{-1}$), respectively, with a corresponding GHe pressure variation from 300 to 1200 kPa. The required system physical properties were evaluated as discussed in Section 3, with $\phi = 0.39775$, $h_{\text{ref}} = 100 \text{ W m}^{-2}\text{K}^{-1}$, and $M_{\text{ref.}} = 1 \text{ kg}$. The mass flow rate in the internal helium channel is not as high as the annular channel which is why only \dot{m}_4 is varied in the analysis. For transient solutions, the initial conditions for the system of ODE given by Eqs. (1), (11), (15), (17), (19), (20), (27) and (28) were $\tau_j^{(i)} = 1$ ($i = 1, \dots, n_{\text{VE}}$; $j = 1, \dots, 9$, $j \neq 7$). For direct steady state solutions,

such values were used as initial guesses.

Fig. 4 shows the mesh convergence study according to Eq. (34). Two different dimensionless mass flow rates settings were used, i.e., $\psi = 86$ ($\dot{m} = 3.8 \text{ g s}^{-1}$) and 147.8 ($\dot{m} = 8.6 \text{ g s}^{-1}$). The analysis reveals that having a mesh with 30 vol elements is sufficient to obtain accurate solutions for the current model.

As pointed out earlier in the text, the model experimental validation was performed using 2 (two) different sets of steady state measured data obtained with different GHe mass flow rates. Initially, set 1 was utilized to investigate the effect of cable operating current on the GHe temperature difference between cryostat inlet and outlet as shown in Fig. 2, which is given by

$$\Delta T_{\text{cryo}} = T_{\text{outlet}} - T_{\text{inlet}} \quad (37)$$

The measured ΔT_{cryo} with respect to cable operating current, i is shown in Fig. 5. For $\dot{m} = 1.4$ ($0 \leq i \leq 2000 \text{ A}$), 3.8 ($0 \leq i \leq 3000 \text{ A}$), and 8.6 ($0 \leq i \leq 3000 \text{ A}$) g s^{-1} , $\Delta T_{\text{cryo}} = 12.49 \pm 0.28$, 5.65 ± 1.00 , and $2.68 \pm 0.13 \text{ K}$, respectively, which shows that the resulting ΔT_{cryo} is robust with respect to cable operating current since the superconducting cable electrical resistance is zero, and therefore no heat generation due to Joule effect. As a result of such observations, set 2 was obtained with no cable current, i.e., $i = 0 \text{ A}$, since no significant differences are expected in ΔT_{cryo} from low to high operating current.

In Fig. 5, the reason why the experiments show a slight temperature rise with increasing current is due to the heat leaks in the terminations, not because of the electrical losses in the HTS cable. For instance, as the HTS DC cable gets longer, that heat generation due to increasing current should remain the same. Also, in DC power cable, there are no transport losses. However, AC cable can have heat generation due to AC loss, which is small compared to the Joule heating or heat leaks in the terminations. The AC loss is a function of frequency and amplitude of the applied power. The characterization of AC loss of the cable is beyond the scope of this paper.

For the experiments performed to obtain set 1, $T_{\text{inlet}} = 51.17 \pm 0.10$, 48.96 ± 1.54 , and $48.70 \pm 0.85 \text{ K}$, for $\dot{m} = 1.4$, 3.8 , and 8.6 g s^{-1} , respectively. The GHe temperature difference between cryostat inlet and outlet, ΔT_{cryo} , was measured in the entire range of tested cable operating currents, and the uncertainty was calculated according to Eq. (36), and the discussion presented in Section 4.2. The largest calculated uncertainty of all measurements was $\frac{U_{\Delta T_{\text{cryo}}}}{\Delta T_{\text{cryo}}} = 0.18$, which is therefore used to plot error bars for all experimental points shown in Figs. 6 and 7.

The model experimental validation initial step was to perform the model adjustment, which consisted of solving the inverse problem of parameters estimation (IPPE) [62], using the mathematical model, i.e., by turning a variable into a parameter, and vice-versa. For that, what was originally a variable is imposed to the model as an input parameter. In this study, the experimentally measured HTS DC cable & cryostat GHe temperature difference, ΔT_{cryo} , for the 3 (three) tested GHe mass flow rates are the imposed variables. The procedure started by selecting the parameters to become the variables to be determined.

The aluminized mylar layer surface emissivity (S6) was selected to be adjusted since it is a function of temperature [50], and the herein utilized emissivity value was measured at 300 K [56]. Additionally, the cryostat heat leak rate through the vacuum space (S7) is very sensitive to the adopted emissivity values of S6 (mylar) and S8 (stainless steel) surfaces. However less inaccuracies are expected from the tabulated stainless steel emissivity values [56]. The temperature field within the cryostat is strongly dependent on the GHe mass flow rate, therefore the available data of set 1 obtained with 3 (three) different GHe mass flow rates were used to adjust the model by inserting constant factors in the mylar emissivity calculations used in Eqs. (22)–(25), as follows:

$$\epsilon_6 = c_i \epsilon_{6,\text{ref}} \quad (38)$$

in which $\epsilon_{6,\text{ref}}$ is S6 (mylar) emissivity at 300 K [56], with $i = 1, 2$ and 3 for $\dot{m} = 1.4, 3.8$ and 8.6 g s^{-1} , respectively. The constants c_i ($i = 1, 2$ and 3) form a vector of adjustment constants to be found. For that, 3

experimental values for ΔT_{cryo} obtained with 3 different GHe mass flow rates from the experimental set 1 were set as parameters in the model, and the 3 constant values were found by solving the IPPE using the mathematical model by trial and error, using the corresponding GHe inlet temperatures. Convergence was assumed when the 3 temperature differences, ΔT_{cryo} , calculated with the mathematical model were within 18% the corresponding experimental values, since the uncertainty of all measurements was evaluated as $\frac{U_{\Delta T_{\text{cryo}}}}{\Delta T_{\text{cryo}}} \leq 0.18$, as explained previously in the text. The final result was $(c_1, c_2, c_3) = (1.8, 2.4, 2.6)^T$. Such values show that as GHe mass flow rate increases c_i tends to stabilize, therefore a fourth degree polynomial is proposed to represent c_i continuously as a function of \dot{m} , for $1.4 \text{ g s}^{-1} \leq \dot{m} \leq 8.6 \text{ g s}^{-1}$, as follows:

$$c_i(\dot{m}) = -3.3936 \times 10^{-4} \dot{m}^4 + 0.010519 \dot{m}^3 - 0.12646 \dot{m}^2 + 0.70804 \dot{m} + 1.029 \quad (39)$$

Fig. 6 shows that the adjusted model simulation line with empty circles lies within the experimental error bars for the entire range of tested GHe mass flow rates for set 1, as expected.

After performing the model adjustment, the next step was the model experimental validation. This task was achieved by using the remaining experimental data set, i.e., set 2. The adjusted model was used to obtain ΔT_{cryo} numerically for the entire range of experimentally tested GHe mass flow rates which were different from set 1, taking the same GHe inlet temperature, T_{inlet} , as the ones observed in the experiments for each tested mass flow rate, which were also different from set 1. The numerically simulated HTS DC cable & cryostat response with respect to the variation of GHe mass flow rate is shown in solid lines with empty circles in Fig. 7. The simulated ΔT_{cryo} curve lies within the error bars for most of the entire tested range. As mass flow rate increases and ΔT_{cryo} decreases, the simulation results are slightly greater than the measured ΔT_{cryo} . It should also be taken into account that the experimental results unexpectedly depict an oscillating behavior as ΔT_{cryo} decreases. Therefore, it is safe to state that there was reasonable quantitative and good qualitative agreement between numerical and experimental results with the use of the adjusted constants correlation proposed by Eq. (39) obtained with set 1, this time for set 2, so that the model could be reliably used to simulate and optimize the HTS DC cable & cryostat response under different geometric and operating conditions.

5.2. HTS DC cable and cryostat simulation and optimization

In order to illustrate the application of the experimentally validated HTS DC cable & cryostat mathematical model, numerical simulations were conducted for assessing the system transient response. The results

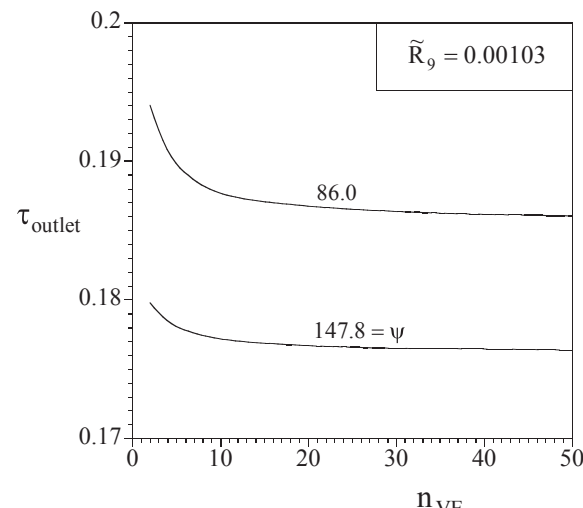


Fig. 4. Mesh convergence assessment.

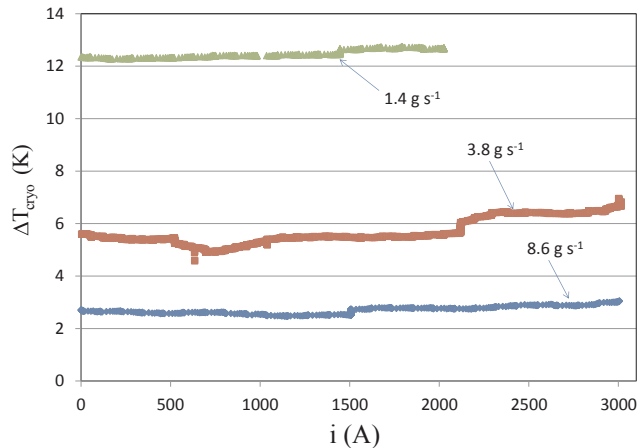


Fig. 5. The effect of HTS DC cable operating current, i , on the GHe temperature difference between cryostat inlet and outlet, ΔT_{cryo} .

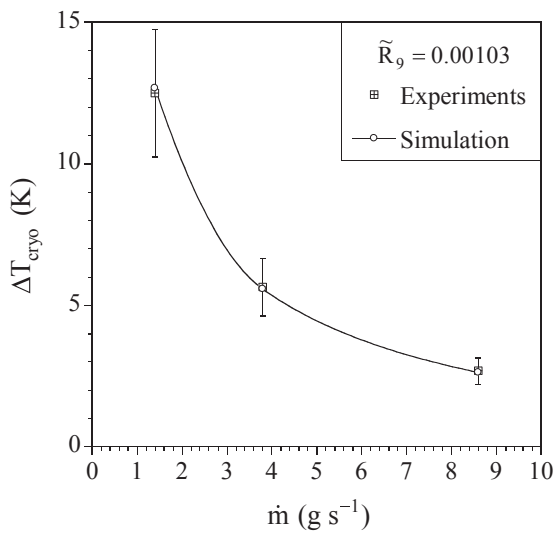


Fig. 6. The model adjustment performed with the GHe temperature difference between cryostat inlet and outlet, ΔT_{cryo} , using set 1 experimental data.

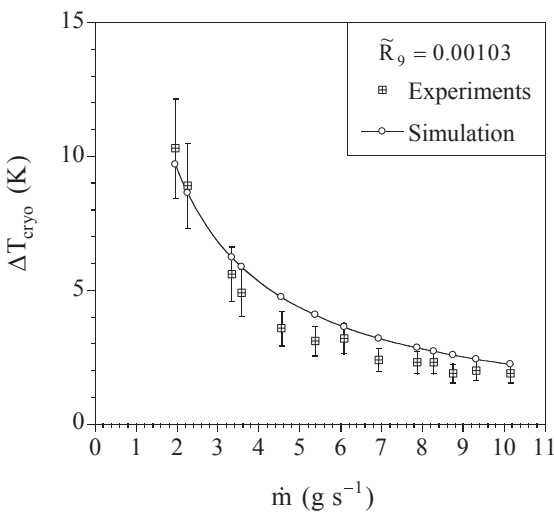
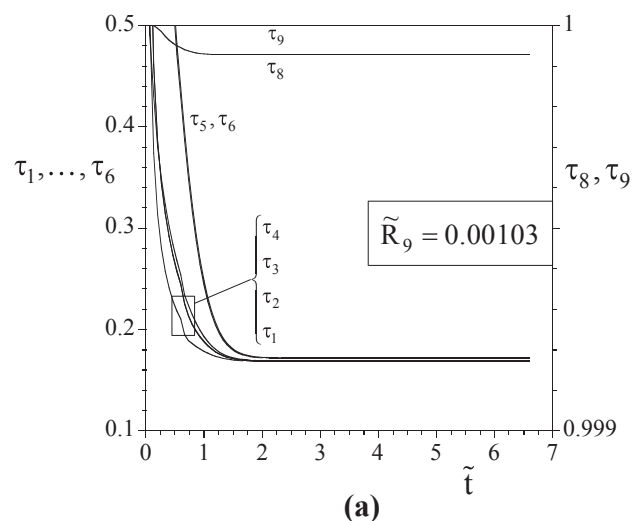
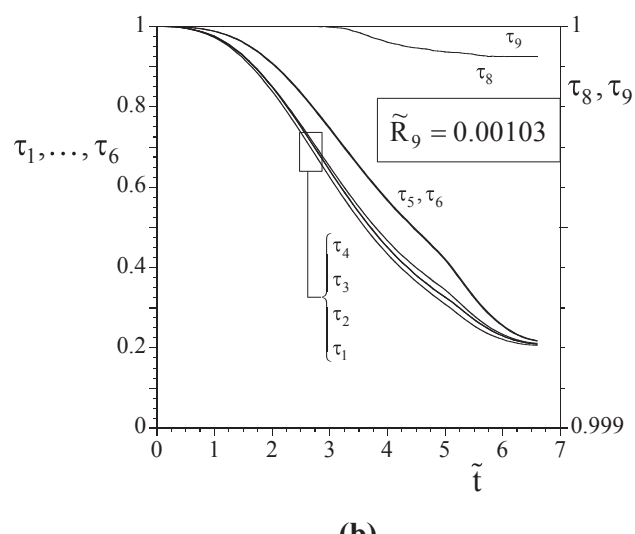


Fig. 7. The model experimental validation performed with the GHe temperature difference between cryostat inlet and outlet, ΔT_{cryo} , using set 2 experimental data.



(a)



(b)

Fig. 8. The cryostat transient dimensionless temperature evolution up to steady state in the first VE (a) and the last VE (b).

shown in Figs. 8 and 9 were obtained for $\dot{m} = 1.4 \text{ g s}^{-1}$ ($\psi = 24.1$), and $T_{\text{inlet}} = 50 \text{ K}$ ($\tau_{\text{inlet}} = 0.168$). Initially, the transient temperature evolution of all layers in Fig. 1 are shown in Fig. 8 in the first and last volume elements, i.e., at $x = 0.5 \text{ m}$ ($\tilde{x} = 0.0167$) and $x = 29.5 \text{ m}$ ($\tilde{x} = 0.9833$), respectively. In the first VE, Fig. 8a shows that the system cools down faster than in the last VE since it is close to the cryostat inlet whereas the last VE is at the end of the cable and receives the warmed coolant that already traveled through the entire cable extracting heat, therefore taking longer than the first VE to achieve the steady state condition. As a result, the last VE determines the system time to achieve steady state, as Fig. 8b shows. The system requires substantial time to reach steady state conditions, which is defined as the system pull-down time, t_{pd} . Also, the results demonstrate the importance of the vacuum layer so that S1 to S6 are kept at temperatures close to the coolant, most importantly S3, the superconducting layer, due to heat transfer only by radiation through S7 which is negligible due to S6 and S8 low emissivity surfaces, and low temperatures. Layers S8 and S9 stabilize at a temperature level close to the ambient temperature. In order to visualize the entire cable thermal response, the steady state temperatures distributions of all layers in Fig. 1 along the cable length are shown in Fig. 9. All layers' temperatures increase monotonically with respect to position along the cryostat.

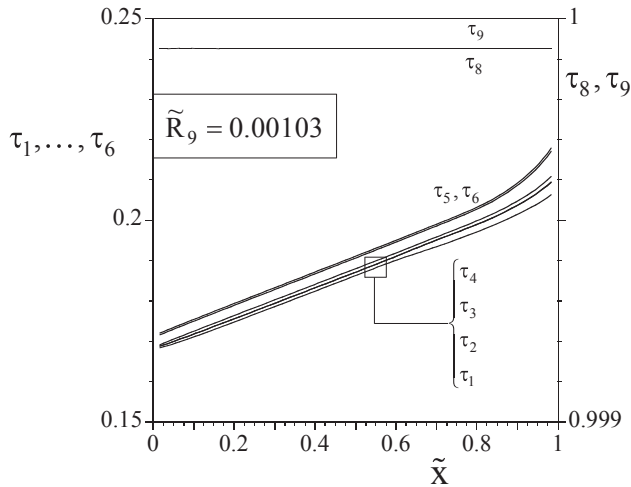


Fig. 9. The cryostat steady state dimensionless temperature distribution.

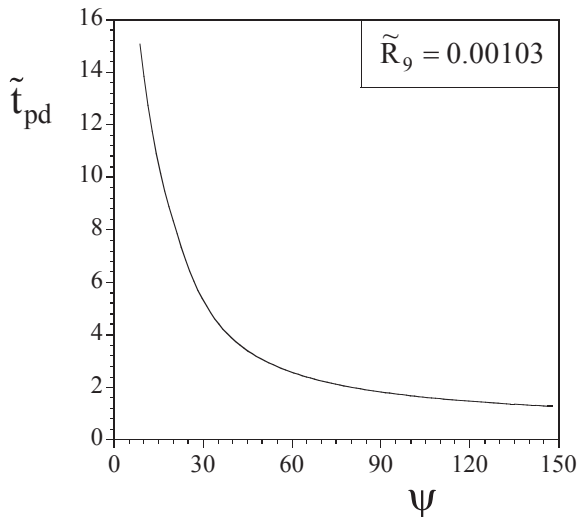


Fig. 10. The system dimensionless pull-down time with respect to dimensionless mass flow rate.

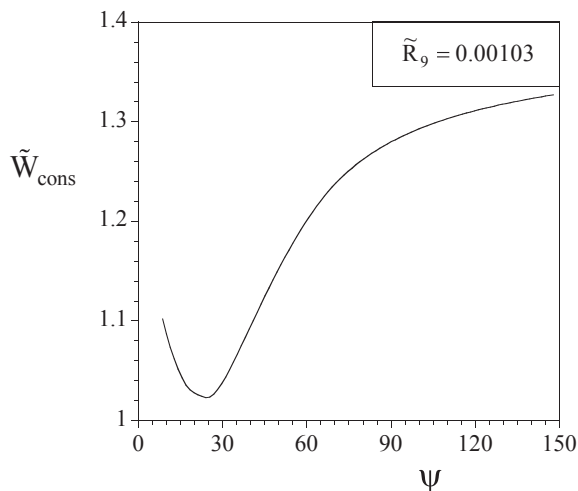


Fig. 11. The minimization of dimensionless total consumed power with respect to dimensionless mass flow rate.

Next, the effect of GHe mass flow rate on pull-down time is investigated in Fig. 10. The lower the mass flow rate the longer it will take for the HTS DC cable & cryostat to reach steady state operation. It is also important to verify that such effect is less pronounced as the GHe mass flow rate increases up to a value from which the pull-down time reduction becomes negligible.

The superconducting cable total consumed power minimization is pursued in Figs. 11 and 12 in steady state operation. As pointed out earlier in the text, in the formulation of the optimization problem, the cryostat cross sectional area ($\tilde{R}_9 = 0.00103$) is kept fixed as a physical constraint in the process. In such circumstances, it is possible to identify operating and design parameters that present trade offs that lead to minimum consumed power. For that, two extremes are analyzed: (i) As ψ decreases, the GHe stream cooling capacity decreases, $\Delta\tau_{cryo}$ increases, thus \tilde{Q}_{cryo} increases, and \tilde{W}_{cons} as well, and (ii) as ψ increases, \tilde{Q}_{cryo} and $\tilde{W}_{fr,tot}$ increase. As a result, an optimal mass flow rate in between the extremes is physically expected, so that \tilde{W}_{cons} is minimized. In fact, Fig. 11 shows that for the HTS DC cable & cryostat geometry of Fig. 1, $\psi_{opt} = 24.1$ for $\tilde{W}_{cons,min} = 1.02$. For $8.6 \leq \psi \leq 147.8$, a 30% variation in \tilde{W}_{cons} was observed, which characterizes a sharp minimum, stressing the importance of system optimal operation.

Finally, a system geometric optimization is sought for different GHe mass flow rate operating conditions. For that, the vacuum jacket dimensions are kept fixed by fixing the S7 to S9 aspect ratio, i.e., $R_7/R_9 = 0.87$, which is the same as the geometry of Fig. 1. Geometrically, trade offs are expected when increasing the GHe annular space at the expense of the vacuum space, and vice versa, thus identifying the annular to vacuum space aspect ratio, R_4/R_7 as the parameter to be optimized. Two extremes are analyzed: (i) As R_4/R_7 decreases, $\tilde{W}_{fr,tot}$ increases, the heat transfer area decreases, $\Delta\tau_{cryo}$ increases, thus \tilde{Q}_{cryo} increases, and \tilde{W}_{cons} as well, and (ii) as R_4/R_7 increases, the vacuum space decreases, thus \tilde{Q}_{cryo} increases. As a result, an optimal annular to vacuum space aspect ratio, R_4/R_7 , in between the extremes is physically expected, so that \tilde{W}_{cons} is minimized. In fact, Fig. 12 shows $(R_4/R_7)_{opt}$ for different operating mass flow rates, depicting sharp minima, $\tilde{W}_{cons,min}$, down to $\psi = 24.1$. For example, for $\psi = 65.3$ ($m = 3.8 \text{ g s}^{-1}$), the cryostat with the original geometry $R_4/R_7 = 0.72$ is shown to consume 20.5% more power than with the optimized geometry $(R_4/R_7)_{opt} = 0.48$.

An interesting result is that a two-way optimization to seek the optimal pair $(R_4/R_7, \psi)_{opt}$ for a two-way minimized consumed power, $\tilde{W}_{cons,min,min}$ is not possible for the geometry of Fig. 1, since the additional constraint $R_4/R_7 > 0.315$ has to be satisfied. However, if the constraint did not exist, such two-way optimized design would not be realistic due to the fact that although $\tilde{W}_{cons,min,min}$ would possibly be found, the two-way optimized ψ would be very low, and $\Delta\tau_{cryo}$ would likely be too high so that the HTS DC cable temperature would surpass the superconducting material critical temperature.

6. Conclusions

In this paper, an HTS DC cable & cryostat dynamic mathematical model with temperature dependence on space was introduced and experimentally validated by direct comparison with measured data from an existing test bed at CAPS-FSU. The HTS DC cable & cryostat total consumed power was obtained numerically with the mathematical model, and the results show good qualitative and quantitative agreement with the values calculated based on measured experimental data. Appropriate dimensionless groups were identified to formulate the model, and the results presented in normalized charts for general application.

The key conclusions of this study are:

- (1) A GHe HTS DC superconducting cable mathematical model has been developed aiming at obtaining fast time and space dependent solutions with the main innovation that solid and fluid components

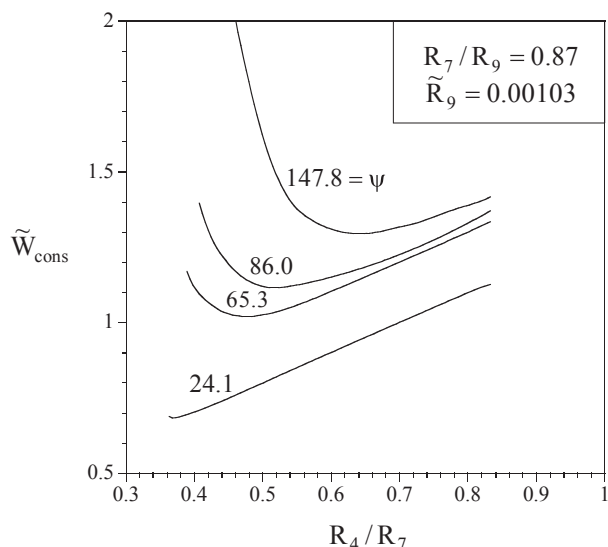


Fig. 12. The minimization of dimensionless total consumed power with respect to annular to vacuum space ratio for different dimensionless mass flow rates.

- coexist in VE in different phases;
- (2) The obtained transient and steady state solutions converge within a timescale on the order of seconds to minutes;
 - (3) The model was adjusted and validated experimentally with reasonable quantitative and good qualitative agreement between numerical and experimental results;
 - (4) Optimal GHe mass flow rate operating condition and geometry were found for minimum total consumed power that lead to significant gains in comparison to existing systems. For example, for a GHe mass flow rate of 3.8 g s^{-1} , the cryostat with the original geometry is shown to consume 20.5% more power than with the optimized geometry, and
 - (5) As a result, it is reasonable to state that the combination of accuracy and low computational time allow for the future utilization of the model as a reliable tool for HTS DC cable & cryostat simulation, control, design and optimization purposes.

Finally, it should be noted that the efficiency of a cryocooler is an important factor in thermal management of HTS systems. However, the coefficient of performance (COP) is largely dependent on operating temperature of the cryocooler. In the calculation of the objective function shown in Eq. (33), the goal was to determine the optimal cryogen fluid operating condition (mass flow rate) for a given inlet temperature. Therefore, the cryocooler COP was not included in Eq. (33), since the purpose of this study was to analyze and minimize the total consumed power of the cable only, not the entire circulation system. For that, the cryocooler efficiency was not important. In future work, for analysis of system-level thermal management, the COP of cryocooler should be included since optimal temperature will vary in the HTS devices and cables in the system.

Acknowledgements

The authors acknowledge with gratitude the support of the Center for Advanced Power systems at Florida State University through the Office of Naval Research, ONR, grant number N00014-16-1-2956, and the National Council for Scientific and Technological Development, CNPq, Brazil, project 302938/2015-0.

Appendix A. Supplementary material

Supplementary data associated with this article can be found, in the

online version, at <https://doi.org/10.1016/j.applthermaleng.2018.08.031>.

References

- [1] T. Hartikainen, J. Lehtonen, R. Mikkonen, Reduction of greenhouse-gas emissions by utilization of superconductivity in electric-power generation, *Appl. Energy* 78 (2004) 151–158, [https://doi.org/10.1016/S0306-2619\(03\)00158-2](https://doi.org/10.1016/S0306-2619(03)00158-2).
- [2] N.G.A. Hemdan, M. Kurrat, T. Schmedes, A. Voigt, R. Busch, Integration of superconducting cables in distribution networks with high penetration of renewable energy resources: Techno-economic analysis, *Int. J. Electrical Power Energy Syst.* 62 (2014) 45–58, <https://doi.org/10.1016/j.ijepes.2014.04.021>.
- [3] J.A. Demko, J.W. Lue, M.J. Gouge, J.P. Stovall, Z. Butterworth, U. Sinha, R. Hughey, Practical AC loss and thermal considerations for HTS power transmission cable systems, *IEEE Trans. Appl. Supercond.* 11 (2001) 1789–1792.
- [4] B.K. Fitzpatrick, J.T. Kephart, E.M. Golda, Characterization of gaseous helium flow cryogen in a flexible cryostat for naval applications of high temperature superconductors, *IEEE Trans. Appl. Supercond.* 17 (2) (2007) 1752–1755.
- [5] J.T. Kephart, B.K. Fitzpatrick, P. Ferrara, M. Pyrt, J. Pienkos, E.M. Golda, High temperature superconducting degaussing from feasibility study to fleet adoption, *IEEE Trans. Appl. Supercond.* 21 (3) (2011) 2229–2232.
- [6] P.J. Ferrara, M.A. Uva, J. Nowlin, Naval ship-to-shore high temperature superconducting power transmission cable feasibility, *IEEE Trans. Appl. Supercond.* 21 (3) (2011) 984–987.
- [7] K.H. Onnes, On the sudden change in the rate at which the resistance of mercury disappears. Communications from the Physical Laboratory of the University of Leiden, 124c (November. 1911), English translation in KNAW Proceedings 1912; 14(2): pp. 818–821.
- [8] C.M. Rey, A.P. Malozemoff, Fundamentals of superconductivity, *Superconductors in the Power Grid: Materials and Applications*, Woodhead Publishing Ltd, Rey CM, Cambridge, UK, 2015, pp. 29–73.
- [9] P. Mangin, R. Kahn, *Superconductivity: An Introduction*, Springer, Cham, 2017.
- [10] L. Duband, A. Ravex, Small cryocoolers, *Handbook of Cryogenic Engineering*, Taylor & Francis, Philadelphia, 1998, pp. 287–320.
- [11] T.P. Beales, J. Jutson, L. Le Lay, M. Mölgg, Comparison of the powder-in-tube processing properties of two $(\text{Bi}_{2-x}\text{Pb}_x)\text{Sr}_2\text{Ca}_2\text{Cu}_3\text{O}_{10+8}$ powders, *J. Mater. Chem.* 7 (4) (1997) 653. <https://doi.org/10.1039/a606896k>.
- [12] A. Schilling, M. Cantoni, J.D. Guo, H.R. Ott, Superconductivity above 130 K in the Hg-Ba-Cu-O system, *Nature* 363 (1993) 56–58.
- [13] R. Thakur, P. Chawla, High temperature superconducting techniques and its applications, *Int. J. Eng. Technol., Manage. Appl. Sci.* 3 (5) (2015) 285–294.
- [14] C.S. Weber, R. Lee, S. Ringo, T. Masuda, H. Yumura, J. Moscovic, Testing and demonstration results of the 350 m long HTS cable system installed in Albany, NY, *IEEE Trans. Appl. Supercond.* 17 (2) (2007) 2038–2042.
- [15] J.F. Maguire, J. Yuan, W. Romanosky, F. Schmidt, R. Soika, S. Bratt, F. Durand, C. King, J. McNamara, T.E. Welsh, Progress and status of a 2G HTS power cable to be installed in the long island power authority (LIPA) grid, *IEEE Trans. Appl. Supercond.* 21 (3) (2011) 961–966.
- [16] H. Yumura, Y. Asheibe, M. Ohya, H. Itoh, M. Watanabe, T. Masuda, H. Ichikawa, T. Mimura, S. Honjo, T. Hara, R. Ohno, M. Shimoda, N. Nakamura, T. Komagome, H. Yaguchi, Update of YOKOHAMA HTS cable project (invited), *IEEE Trans. Appl. Supercond.* 23 (3) (2013) 5402306.
- [17] C. Ryu, H. Jang, Y. Teng, X. Liang, N. Song, Z. Cao, Z. Zhu, Z. Gao, T. Ma, D. Zhang, F. Zhang, Z. Zhang, X. Xu, L. Lin, Current status of demonstration and commercialization of HTS cables system in grid in Korea, in: *IEEE International Conference on Applied Superconductivity and Electromagnetic Devices (ASEMD)*, 2013, pp. 539–542.
- [18] L. Xiao, S. Dai, L. Lin, Z. Zhang, J. Zhan, HTS power technology for future DC power grid (invited), *IEEE Trans. Appl. Supercond.* 23 (3) (2013) 5401506.
- [19] S. Dai, L. Xiao, H. Zhang, Y. Teng, X. Liang, N. Song, Z. Cao, Z. Zhu, Z. Gao, T. Ma, D. Zhang, F. Zhang, Z. Zhang, X. Xu, L. Lin, Testing and demonstration of a 10-kA HTS DC power cable, *IEEE Trans. Appl. Supercond.* 24 (2) (2014) 5400104.
- [20] F. Herzog, T. Kutz, M. Stemmle, T. Kugel, Cooling unit for the Ampa City project - One year successful operation, *Cryogenics* 80 (2) (2016) 204–209.
- [21] D. Ding, Z. Pan, D. Cuiuri, H. Li, Wire-feed additive manufacturing of metal components: technologies, developments and future interests, *Int. J. Adv. Manuf. Technol.* 81 (1) (2015) 465–481.
- [22] S. Lee, V. Petrykin, A. Molodyk, S. Samoilenkova, A. Kaul, A. Vavilov, V. Vysotsky, S. Fetisov, Development and production of second generation high Tc superconducting tapes at SuperOr and first tests of model cables, *Superconductor Sci. Technol.* 27 (4) (2014) Art. ID 044022.
- [23] P. Li, D. Abraimov, A. Polyanskiy, F. Kametani, D. Larbalestier, Study of grain boundary transparency in $(\text{Yb}_{1-x}\text{Ca}_x)\text{Ba}_2\text{Cu}_3\text{O}$ bicrystal thin films over a wide temperature, field, and field orientation range, *Phys. Rev. B* 91 (10) (2015) Art. ID 104504.
- [24] L. Rossi, X. Hu, F. Kametani, D. Abraimov, A. Polyanskiy, J. Jarosynski, D.C. Larbalestier, Sample and length-dependent variability of 77 and 4.2 K properties in nominally identical RE123 coated conductors, *Superconductor Sci. Technol.* 29 (5) (2016) Art. ID 054006.
- [25] A. Xu, N. Khatri, Y. Liu, G. Majkic, E. Galstyan, V. Selvamanickam, Y. Chen, C. Lei, D. Abraimov, X. Hu, J. Jarosynski, D. Larbalestier, Broad temperature pinning study of 15 mol.% Zr-Added (Gd, Y)-Ba-Cu-O MOCVD Coated Conductors, *IEEE Trans. Appl. Supercond.* 25 (3) (2015) 1–5.
- [26] S. Eckroad, Novel Approaches and Alternative Cryogens for Cooling a

- Superconducting Cable: a Comparison of Liquid Air with Other Fluids, EPRI, Palo Alto, CA, 2012, p. 1025813.
- [27] J.A. Demko, W.V. Hassenzahl, Thermal management of long-length HTS Cable Systems, *IEEE Trans. Appl. Supercond.* 21 (3) (2011) 957.
- [28] M. Wozniak, L. Bromberg, B.A. Glowacki, J. Xiaohua, Z. Rong, J.V. Minervini, J.G. Brisson, DC superconducting cable using MgB₂ wires, *IEEE Trans. Appl. Supercond.* 23 (3) (2013) 6200805.
- [29] EPRI, Program on technology innovation: a superconducting DC cable, Electric Power Research Institute Inc, Palo Alto, 2009.
- [30] S. Pamidi, C.H. Kim, L. Gruber, High-temperature superconducting (HTS) power cables cooled by helium gas, *Superconductors in the Power Grid: Materials and Applications*, Woodhead Publishing Ltd., Rey C, Cambridge, UK, 2015, pp. 225–260.
- [31] B.K. Fitzpatrick, J.T. Kephart, E.M. Golda, Characterization of gaseous helium flow cryogen in a flexible cryostat for naval applications of high temperature superconductors, *IEEE Trans. Appl. Supercond.* 17 (2) (2007) 1752–1755.
- [32] J.T. Kephart, B.K. Fitzpatrick, P. Ferrara, M. Pyryt, J. Miller, C. Nadig, Flow resistance experiments in HTS cable form, *IEEE Trans. Appl. Supercond.* 23 (3) (2013) 4.
- [33] J. Miller, D. Santosusso, M. Uva, K. Woods, B. Fitzpatrick, Naval Superconducting Integrated Power System (SIPS), Intelligent Ship Symposium, 2013.
- [34] L. Gruber, C.H. Kim, S.V. Pamidi, H. Rodrigo, D. Knoll, Dielectric design validation of a helium gas cooled superconducting DC power cable, in: Electrical Insulation Conference (EIC), Philadelphia, PA, 2014.
- [35] L. Gruber, J.G. Kim, C.H. Kim, S. Pamidi, Thermal network model for HTS cable systems and components cooled by helium gas, *IEEE Trans. Appl. Supercond.* 26 (4) (2016) 4803805.
- [36] L. Gruber, N. Sutell, D. Shah, D.G. Crook, C.H. Kim, J.C. Ordóñez, S. Pamidi, Cryogenic heat sink for helium gas cooled superconducting power devices, COMSOL Technical Papers and Presentations, 2012.
- [37] S.V. Pamidi, C.H. Kim, D. Crook, S. Dale, Cryogenic helium gas circulation system for advanced characterization of superconducting cables and other devices, *Cryogenics* 52 (4) (2012) 315–320.
- [38] J.Y. Xu, J.Y. Hu, L.M. Zhang, E.C. Luo, A novel shell-tube water-cooled heat exchanger for high-capacity pulse-tube coolers, *Appl. Therm. Eng.* 106 (2016) 399–404, <https://doi.org/10.1016/j.applthermaleng.2016.06.020>.
- [39] D. Shah, J.C. Ordóñez, C.H. Kim, L. Gruber, N. Sutell, J.V.C. Vargas, S.V. Pamidi, Cryogenic thermal modeling and experimental validation of a novel heat sink for helium gas cooled superconducting devices, *IEEE Trans. Appl. Supercond.* 25 (3) (2015) Art ID: 0600204.
- [40] C.H. Kim, S.K. Kim, L. Gruber, S.V. Pamidi, Cryogenic thermal studies on terminations for helium gas cooled superconducting cables, *Phys. Procedia* 67 (2015) 201–207.
- [41] P. Cheetham, W. Kim, C.H. Kim, S.V. Pamidi, L. Gruber, H. Rodrigo, Use of partial discharge inception voltage measurements to design a gaseous helium cooled high temperature superconducting power cable, *IEEE Trans. Dielectr. Electr. Insul.* 24 (1) (2017) 191–199.
- [42] J.C. Ordóñez, J.A. Souza, D.R. Shah, J.V.C. Vargas, R. Hovsepian, Temperature and pressure drop model for gaseous helium cooled superconducting DC cables, *IEEE Trans. Appl. Supercond.* 23 (3) (2013) 5402005.
- [43] H. Rodrigo, F. Salmoher, D.S. Kwag, S.V. Pamidi, L. Gruber, D.G. Crook, S.L. Ranner, S.J. Dale, D. Knoll, Electrical and thermal characterization of a novel high pressure gas cooled DC power cable, *Cryogenics* 52 (4) (2012) 310–314.
- [44] J.A. Demko, J.W. Lue, M.J. Gouge, J.P. Stovall, Z. Butterworth, U. Sinha, R. Hughey, Practical AC loss and thermal considerations for HTS power transmission cable systems, *IEEE Trans. Appl. Supercon.* 11 (1) (2001) 1789–1792.
- [45] J.A. Souza, J.C. Ordóñez, R. Hovsepian, J.V.C. Vargas, Thermal modeling of helium cooled high-temperature superconducting DC transmission cable, *IEEE Trans. Appl. Supercond.* 31 (3) (2011) 947–952, <https://doi.org/10.1109/TASC.2010.2099196>.
- [46] F.P. Incropera, D.P. DeWitt, T.L. Bergman, A.S. Lavine, *Fundamentals of Heat and Mass Transfer*, John Wiley & Sons, 2010.
- [47] A. Bejan, *Convection Heat Transfer*, third ed., Wiley, New York, 2004.
- [48] H. Tatsumoto, Y. Shirai, K. Hata, T. Kato, T. Aso, K. Ohtsu, M. Shiootsu, Numerical analysis of forced convection heat transfer of subcooled liquid nitrogen, *IEEE Trans. Appl. Supercond.* 18 (2008) 1483–1486.
- [49] P.G. Vicente, A. García, A. Viedma, Experimental investigation on heat transfer and frictional characteristics of spirally corrugated tubes in turbulent flow at different Prandtl numbers, *Int. J. Heat Mass Transf.* 47 (2004) 671–681.
- [50] R. Siegel, J.R. Howell, *Thermal Radiation Heat Transfer*, third ed., Taylor & Francis, Washington, 1992.
- [51] V.D. Arp, R.D. McCarty, D.G. Friend, Thermophysical properties of helium-4 from 0.8 to 1500 K with pressures to 2000 MPa, *Natl. Inst. Stand. Technol., Tech. Note* 1334 (revised), 152 pages, September 1998.
- [52] S.W. Akin, The thermodynamic properties of helium, *Trans. ASME* 72 (1954) 751–757.
- [53] LNG Materials and Fluids. Ed. Douglas Mann, National Bureau of Standards, Cryogenics Division, First Edition, 1977.
- [54] C.L. Choy, D. Grieg D. The low temperature thermal conductivity of a semi-crystalline polymer, polyethylene terephthalate, *J. Phys. C: Solid State Phys.* 8 (19) (1975) 3121–3129.
- [55] Dupont, Mylar® polyester film Physical-Thermal Properties, Product Information 222367D, Printed in U.S.A. [Replaces: H-37232-2] Reorder No.: H-37232-3, 2003.
- [56] J.H. Henninger, Solar absorptance and thermal emittance of some common spacecraft thermal control coatings, NASA Reference Publication 1121, April 1984.
- [57] A.D. Berger, Stability of superconducting cables with twisted stacked YBCO coated conductors, PSFC/RR-11-15, Plasma Science and Fusion Center, Massachusetts Institute of Technology, Cambridge, MA, 2012.
- [58] D. Kincaid, W. Cheney, *Numerical Analysis*, Wadsworth, Belmont, CA, USA, 1991.
- [59] Editorial Board, Journal of heat transfer editorial policy statement on numerical accuracy, *ASME J. Heat Transfer* 116 (1994) 797–798.
- [60] G. van Belle, *Statistical Rules of Thumb*, second ed., Wiley-Interscience, New York, USA, 2008.
- [61] J.H. Kim, T.W. Simon, R. Viskanta, Journal of heat transfer policy on reporting uncertainties in experimental measurements and results (editorial), *J. Heat Transfer* 115 (1993) 5–6.
- [62] W.J. Minkowycz, E.M. Sparrow, G.E. Schneider, R.H. Pletcher, *Handbook of Numerical Heat Transfer*, second ed., Wiley, New York, USA, 2006 Chapter 17.